

# Lagrangian stretching reveals stress topology in viscoelastic flows

Manish Kumar<sup>a</sup>, Jeffrey S. Guasto<sup>b</sup>, and Arezoo M. Ardekani<sup>a,1</sup>

Edited by Harry Swinney, University of Texas, Austin, TX; received July 6, 2022; accepted November 1, 2022

Viscoelastic flows are pervasive in a host of natural and industrial processes, where the emergence of nonlinear and time-dependent dynamics regulates flow resistance, energy consumption, and particulate dispersal. Polymeric stress induced by the advection and stretching of suspended polymers feeds back on the underlying fluid flow, which ultimately dictates the dynamics, instability, and transport properties of viscoelastic fluids. However, direct experimental quantification of the stress field is challenging, and a fundamental understanding of how Lagrangian flow structure regulates the distribution of polymeric stress is lacking. In this work, we show that the topology of the polymeric stress field precisely mirrors the Lagrangian stretching field, where the latter depends solely on flow kinematics. We develop a general analytical expression that directly relates the polymeric stress and stretching in weakly viscoelastic fluids for both nonlinear and unsteady flows, which is also extended to special cases characterized by strong kinematics. Furthermore, numerical simulations reveal a clear correlation between the stress and stretching field topologies for unstable viscoelastic flows across a broad range of geometries. Ultimately, our results establish a connection between the Eulerian stress field and the Lagrangian structure of viscoelastic flows. This work provides a simple framework to determine the topology of polymeric stress directly from readily measurable flow field data and lays the foundation for directly linking the polymeric stress to flow transport properties.

Lagrangian stretching | viscoelastic flow | polymeric stress | elastic instability

The stretching of long-chain polymers in flow imparts viscoelastic properties to fluids, which impact diverse industrial, geophysical, and biological applications (1-4). Viscoelasticity leads to increased flow resistance in enhanced oil recovery, polymer processing, and microbial mining (5-7), and it enhances fluid and particulate transport in targeted drug delivery and reproduction (8-10). Extensional flow components simultaneously stretch and advect polymeric chains, which creates large and inhomogeneously distributed polymeric stress (11). Viscoelastic instabilities occur (12, 13) when elastic stresses dominate viscous stresses and manifest symmetry breaking (14), time-dependent flow (15), and enhanced mixing (16). The onset of these phenomena is captured by the Weissenberg number (Wi), representing the ratio of elastic to viscous stress: Wi =  $\lambda \dot{\gamma}$ , where  $\lambda$  and  $\dot{\gamma}$  are the polymeric relaxation time and deformation rate, respectively. Importantly, the topology of the polymeric stress field has been shown to regulate flow structure, whereby streaks of high polymeric stress lead to separation and act as a barrier to flow (17, 18). Determining the topology of the stress field and its relationship to flow kinematics is fundamental to understanding and predicting dynamic flow patterns and, ultimately, material transport in complex flows.

Direct optical measurements of the stress field and polymer deformation in viscoelastic flows are challenging (19, 20). Flow-induced birefringence measurements can provide spatially resolved stress fields, but they require highly specialized imaging instruments (21, 22). Furthermore, large stress-optical coefficients are difficult to achieve for polymeric solutions (20, 23), and the linear stress-optical rule is not applicable at high stress (20, 24). Individual polymer stretching measurements (25, 26) are possible, but they require singlemolecule imaging sensitivity, do not provide whole-field information, and are limited to relatively slow flows. However, recognizing that the polymeric stress distribution is inherently coupled to polymer advection and deformation through flow kinematics suggests that a Lagrangian analysis of viscoelastic flows can provide direct insight into the structure of the polymeric stress field.

The Lagrangian stretching field is a type of Lagrangian coherent structure (LCS) (27– 29) that has found numerous applications in geophysical flows (29), active and passive particle transport (30, 31), and chemical reacting flows, but its use in non-Newtonian flows has been limited (32). The stretching field quantifies the relative deformation of

### **Significance**

Viscoelastic flows are common in biological, geological, and industrial processes, where polymer stretching leads to unstable, time-dependent flows and anomalous transport properties. Quantifying the local polymeric stress is essential to forecasting the onset of such flow instabilities as well as their impact on mixing applications, but direct measurements of the stress field are challenging. A Lagrangian analysis of fluid kinematics establishes a fundamental connection with the Eulerian stress field in viscoelastic flows. These results provide a framework to determine the stress topology directly from conventional experimental flow measurements for arbitrary viscoelastic fluids and flows, including 3D geometries and unsteady flows.

Author affiliations: a Department of Mechanical Engineering, Purdue University, West Lafayette, IN 47907; and <sup>b</sup>Department of Mechanical Engineering, Tufts University, Medford, MA 02155

Author contributions: M.K., J.S.G., and A.M.A. designed research; M.K., and A.M.A. performed research; M.K., J.S.G., and A.M.A. analyzed data; and M.K., J.S.G., and A.M.A. wrote the paper.

The authors declare no competing interest.

This article is a PNAS Direct Submission

Copyright © 2023 the Author(s). Published by PNAS. This article is distributed under Creative Commons Attribution-NonCommercial-NoDerivatives License 4.0 (CC BY-NC-ND).

<sup>1</sup>To whom correspondence may be addressed. Email: ardekani@purdue.edu.

This article contains supporting information online at http://www.pnas.org/lookup/suppl/doi:10.1073/pnas. 2211347120/-/DCSupplemental.

Published January 26, 2023.

fluid elements in flow, but unlike the polymeric stress, it is easily computed from readily measurable velocity fields (29). Therefore, in this work, we determine the relationship between the polymeric stress and the Lagrangian stretching field for a broad range of viscoelastic fluid flows. In the limit of small Weissenberg number (Wi « 1), theoretical analysis yields a general analytical expression that directly relates the trace of the polymeric stress tensor to the stretching field, which applies even in unsteady and nonlinear flows and is extended to special cases (33) exhibiting strong kinematics (Wi  $\gg$  1). Further, numerical simulations at large Weissenberg numbers (Wi  $\gtrsim 1)$  demonstrate the strong correlation between the stretching and stress fields in nontrivial geometries and highly time-dependent, chaotic flows. Taken together, these results fundamentally establish how the Lagrangian flow structure underpins the Eulerian stress distribution in viscoelastic flows. They also provide a framework to determine the polymeric stress field topology for arbitrary flows, which will ultimately provide insights into the onset of viscoelastic instabilities and their transport properties.

### **Results and Discussion**

Lagrangian Stretching and Polymeric Stress Fields for Weakly Viscoelastic Flows. In the limit of small Weissenberg number (Wi  $\ll$  1), we first derive an analytical relationship between the trace of the polymeric stress tensor and the Lagrangian stretching field for simple, linear flows. The Lagrangian stretching field quantifies the relative elongation of a fluid element during advection and deformation in flow over a fixed time interval (28). To determine the stretching field, material lines in the velocity field,  $\mathbf{u}$ , are first obtained by integrating  $\frac{d\mathbf{x}}{dt} = \mathbf{u}(\mathbf{x}, t)$ . The solution is denoted as the flow map,  $\mathbf{\Phi} = \mathbf{x}(t_1, \mathbf{x}_0, t_0)$ , which provides a mapping between the initial,  $x_0$ , and final positions of fluid particles due to advection between times  $t_0$  and  $t_1$ . The Lagrangian history of fluid particle deformation is encoded in the gradients of the flow map and represented by the right Cauchy-Green strain tensor

$$\mathbf{C}_R = (\nabla \mathbf{\Phi})^\mathsf{T} \nabla \mathbf{\Phi},$$
 [1]

which is symmetric. The Lagrangian stretching field,  $S(\mathbf{x}, t)$ , is defined as the square root of the largest eigenvalue of  $\mathbf{C}_R$ (28) and the corresponding eigenvector indicates the direction of stretching (30). The stretching field is calculated analytically for simple flow fields and numerically for simulated or measured flows, where the time interval,  $\Delta t = t_0 - t_1$ , is chosen based on the natural flow time scale. For viscoelastic flows, the local polymeric stress at a particular time depends directly on the accrued stretching of the polymeric chains over the course of their relaxation time. Thus, to develop a correlation between the polymeric stress and Lagrangian stretching fields, we examine S over the time interval  $\Delta t = \lambda$  (unless specified otherwise), which

represents the relevant time scales for both polymer stretching and relaxation.

In the case of Wi  $\ll$  1, various models for viscoelastic fluids converge to the second-order fluid model (34), and the polymeric stress tensor is given as

$$\tau_p = b_1 \gamma_{(1)} + b_2 \gamma_{(2)} + b_{11} \{ \gamma_{(1)} \cdot \gamma_{(1)} \},$$
 [2]

where  $b_1$  is the polymeric contribution to the viscosity, and  $b_2$ and  $b_{11}$  represent the first and second normal stress differences, respectively. For the second-order fluid model, the polymeric relaxation time can be given as  $\lambda = -b_2/b_1$  (SI Appendix, Table S1) (34). For weakly viscoelastic fluids, the stress tensor is calculated using the Newtonian velocity field via Giesekus's theorem (34).  $\gamma_{(1)} = \nabla \mathbf{u} + (\nabla \mathbf{u})^{\mathsf{T}}$  is the strain rate tensor, and its higher-order derivatives are obtained from the following relationship:

$$\boldsymbol{\gamma}_{(n+1)} = \frac{D\boldsymbol{\gamma}_n}{Dt} - \{(\nabla \mathbf{u})^\mathsf{T} \cdot \boldsymbol{\gamma}_n + \boldsymbol{\gamma}_n \cdot (\nabla \mathbf{u})\}, \quad [3]$$

where  $\frac{D}{Dt} = \frac{\partial}{\partial t} + \mathbf{u} \cdot \nabla$  is the material derivative. For linear extensional, shear, and rotational flows, the trace of the stress tensor,  $tr(\tau_p)$ , and the stretching field, S, were both calculated analytically and are both spatially uniform due to constant  $\nabla \mathbf{u}$ and  $\nabla \Phi$ , respectively. The results are summarized in Table 1. In the special case of uniform (rigid body) motion, for example, in a rotational flow, the trace of the stress tensor is  $tr(\tau_p) = 0$  due to a lack of fluid deformation. Likewise, S = 1 as it represents the relative elongation of a fluid element, and the net stretching is S-1. For linear flows (Table 1),  $tr(\tau_p)$  and S satisfy the following equation for Wi  $\ll 1$ :

$$\operatorname{tr}(\boldsymbol{\tau_p}) = \frac{2(b_{11} - b_2)}{\lambda^2} (S^2 - 1)^2.$$
 [4]

The stretching field has the form S = 1 + O(Wi). Therefore, any power of S can be written as  $S^n = 1 + nO(Wi)$  to leading order, which gives the general equation:

$$tr(\boldsymbol{\tau_p}) = \frac{8}{n^2} \frac{(b_{11} - b_2)}{\lambda^2} (S^n - 1)^2,$$
 [5]

where  $n \neq 0$ . The simplicity of this result suggests that the stretching and stress fields are intrinsically linked.

## Extension to Nonlinear Flows with Weakly Viscoelastic Fluids.

The simple linear flows explored above provide important insights into the relationship between homogeneous polymer stress and stretching fields, but whether such relationships (Eq. 5) hold for topologically complex flows with spatially varying velocity gradients remains to be determined. Therefore, we derive  $tr(\tau_p)$  and S for a series of spatially nonlinear flows at

Analytical polymeric stress and stretching fields for small Weissenberg number (Wi  $\ll$  1) linear flows Table 1.

| Flow type         | Velocity field ( <b>u</b> )                    | Stress field ( $\operatorname{tr}(\pmb{	au_p})$ )  | Stretching field (S)   |
|-------------------|--|--|--|
| Extensional flow  | $u = \dot{\epsilon} x,  v = -\dot{\epsilon} y$ |  | $S^2 = e^{2Wi} = 1 + 2Wi + 2Wi^2 + H.O.T.$   |
| Simple shear flow | $u = \dot{\gamma}y$ , $v = 0$                  | $\operatorname{tr}(\boldsymbol{\tau_p}) = \frac{2(b_{11} - b_2)}{\lambda^2} \operatorname{Wi}^2$ | $S^2 = 1 + \frac{1}{2}Wi^2 + Wi\left(1 + \frac{1}{4}Wi^2\right)^{1/2} = 1 + Wi + \frac{1}{2}Wi^2 + H.O.T.$ |
| Rotational flow   | $u = -\Omega y$ , $v = \Omega x$               | $\operatorname{tr}(\pmb{	au_p}) = 0$   | $S^2 = 1$  |

Weissenberg numbers (Wi) for extensional and shear flows are defined as  $Wi = \dot{\epsilon}\lambda$  and  $Wi = \dot{\gamma}\lambda$ , respectively. Stretching fields (S) are determined exactly and also shown in terms of the Taylor expansion up to  $O(Wi^2)$  with the remaining terms indicated by H.O.T.

Wi  $\ll$  1. In a Poiseuille flow through a channel of height 2H with center-line flow speed  $U_0$  and velocity field components,  $u = U_0[1 - (y/H)^2]$  and v = 0,  $\operatorname{tr}(\tau_p)$  and S are given by

$$tr(\boldsymbol{\tau_p}) = \frac{8(b_{11} - b_2)}{\lambda^2} \bar{y}^2 \text{Wi}^2,$$

$$S^2 = 1 + 2\bar{y}^2 \text{Wi}^2 + 2\bar{y} \text{Wi} \left(1 + \bar{y}^2 \text{Wi}^2\right)^{1/2}$$

$$= 1 + 2\bar{y} \text{Wi} + 2\bar{y}^2 \text{Wi}^2 + \text{H.O.T.},$$
[7]

where Wi =  $U_0\lambda/H$  and  $\bar{y} = |y|/H$ . Next, we consider a quadratic extensional flow with  $u = \dot{\epsilon}_1 xy$  and  $v = -\frac{1}{2}\dot{\epsilon}_1 y^2$ . The resulting stress and stretching were found to be

$$tr(\boldsymbol{\tau_p}) = \frac{2(b_{11} - b_2)}{\lambda^2} (\bar{x}^2 + 4\bar{y}^2) \text{Wi}^2,$$

$$S^2 = 1 + (\bar{x}^2 + 4\bar{y}^2)^{1/2} \text{Wi}$$

$$+ \frac{1}{2} \left\{ (\bar{x}^2 + 4\bar{y}^2) + \left( \frac{2\bar{y}^3 - \bar{y}\bar{x}^2}{\sqrt{\bar{x}^2 + 4\bar{y}^2}} \right) \right\} \text{Wi}^2 + \text{H.O.T.},$$
[9]

where Wi =  $\dot{\epsilon}_1 L_c \lambda$ ,  $\bar{x} = x/L_c$ ,  $\bar{y} = y/L_c$ , and  $L_c$  is the characteristic length scale of flow. The two quadratic flow fields examined above exhibit spatially nonuniform stretching and stress fields. However, the relationship between  $\text{tr}(\tau_p)$  and S derived in Eq. 5 for linear flows also holds for nonlinear flows. As further validation, we consider the quartic extensional velocity field  $u = \frac{1}{2} \dot{\epsilon}_2 x^2 y^2$  and  $v = -\frac{1}{3} \dot{\epsilon}_2 x y^3$  and analytically derive  $\text{tr}(\tau_p)$  and S:

$$\operatorname{tr}(\boldsymbol{\tau_p}) = \frac{2(b_{11} - b_2)}{\lambda^2} \left( \bar{x}^4 \bar{y}^2 + \frac{10}{3} \bar{x}^2 \bar{y}^4 + \frac{1}{9} \bar{y}^6 \right) \operatorname{Wi}^2, \quad [10]$$

$$S^2 = 1 + \left( \bar{x}^4 \bar{y}^2 + \frac{10}{3} \bar{x}^2 \bar{y}^4 + \frac{1}{9} \bar{y}^6 \right)^{1/2} \operatorname{Wi}$$

$$+ \frac{1}{2} \left\{ \begin{array}{l} \left( \bar{x}^4 \bar{y}^2 + \frac{10}{3} \bar{x}^2 \bar{y}^4 + \frac{1}{9} \bar{y}^6 \right) + \\ \frac{1}{3} \left( \frac{-6 \bar{x}^5 \bar{y}^4 + 5 \bar{x}^3 \bar{y}^6 + \bar{x} \bar{y}^8}{\sqrt{9 \bar{x}^4 \bar{y}^2 + 30 \bar{x}^2 \bar{y}^4 + \bar{y}^6}} \right) \end{array} \right\} \operatorname{Wi}^2 + \operatorname{H.O.T.},$$

$$[11]$$

where Wi =  $\dot{\epsilon}_2 L_c^3 \lambda$ . Strikingly, the expression established in Eq. **5** also holds for the quartic extensional flow.

**Extension to Weakly Unsteady Viscoelastic Flows.** To expand the applicability of the relationship between polymeric stress and stretching, we next extend our analysis to time-dependent flows. Viscoelastic flows are fully characterized not just by Wi but also by the dimensionless Deborah number ( $De = \lambda/T$ ). The latter is a measure of unsteadiness and corresponds to the ratio of polymeric relaxation time ( $\lambda$ ) to the characteristic time scale of the flow (T) (35). For weakly viscoelastic (Wi  $\ll$  1) and weakly unsteady ( $De \ll$  1) flows, we consider a time-dependent perturbation to a velocity field,  $\mathbf{u} = \mathbf{u_0}[1 + De \alpha(t)]$ , where  $\mathbf{u_0}$  is a steady linear or nonlinear flow (e.g., explored in the previous sections), and  $\alpha(t)$  is an arbitrary time-dependent function. Under these conditions, the ordered fluid model (Eq. 2) is still applicable (34, 36), and we find that the instantaneous stress and stretching fields (i.e.,  $t = t_0$ ) satisfy the following relationship (*SI Appendix*):

$$tr(\boldsymbol{\tau_p}) = \frac{8}{n^2} \frac{(b_{11} - b_2)}{\lambda^2} g_1(t_0) (S^n - 1)^2,$$
 [12]

where

$$g_1(t_0) = \left\lceil \frac{1 + \text{De}\alpha(t_0)}{1 + \text{De}\beta(t_0)} \right\rceil^2, \quad [13]$$

and  $\beta(t_0) = -\frac{1}{\lambda} \int_{t_0}^{t_0 - \lambda} \alpha(t) dt$ .

In the special case of fluid motions with constant stretch history (MWCSH) (33, 37–39)—for example, linear and Poiseuille flows—the stress tensor can be obtained using the first three kinematic tensors ( $\gamma_{(1)}, \gamma_{(2)}$ , and  $\gamma_{(3)}$ ) (40). For Wi < 1, the leading-order term (i.e., O(Wi)) of the stretching field still dominates. Thus, for weakly modulated MWCSH flows (De  $\ll$  1), the relationship between the stress and stretching fields at Wi < 1 is described by Eq. 12 (replace  $g_1$  with  $g_2$ ), where specifically (*SI Appendix*)

$$g_2(t_0) = \frac{\left[ \{1 + \operatorname{De}\alpha(t_0)\}^2 + \frac{2b_{12} - 3b_3}{\lambda(b_{11} - b_2)} \{1 + \operatorname{De}\alpha(t_0)\} \operatorname{De}\zeta(t_0) \right]}{\left[1 + \operatorname{De}\beta(t_0)\right]^2},$$

 $\zeta(t_0) = \lambda \alpha'(t_0)$ , and  $b_3$  and  $b_{12}$  are the constants associated with the third-order kinematic tensors. We note that in the limit of De  $\rightarrow$  0,  $g_{1,2}(t_0) \rightarrow$  1 and Eq. 12 converges to Eq. 5 for steady flows. Furthermore, the stress fields obtained for flows undergoing MWCSH are applicable for all Wi. For strong kinematics (Wi  $\gg$  1), the highest-order (i.e.,  $O(\text{Wi}^2)$ ) term of the stretching field dominates in shear flows. Therefore, the relationship between the stress and stretching fields at Wi  $\gg$  1 for weakly modulated (De  $\ll$  1) homogeneous (simple shear) and nonhomogeneous (Poiseuille) shear flows is:

$$tr(\tau_p) = 2 \frac{(b_{11} - b_2)}{\lambda^2} g_2(t_0) S^2.$$
 [15]

In contrast, the linear extensional flow at Wi  $\gtrsim 1$  and De  $\ll 1$  satisfies a different relationship (*SI Appendix*):

$$\operatorname{tr}(\boldsymbol{\tau}_{\boldsymbol{p}}) = 8 \frac{(b_{11} - b_2)}{\lambda^2} g_2(t_0) (\ln(S))^2.$$
 [16]

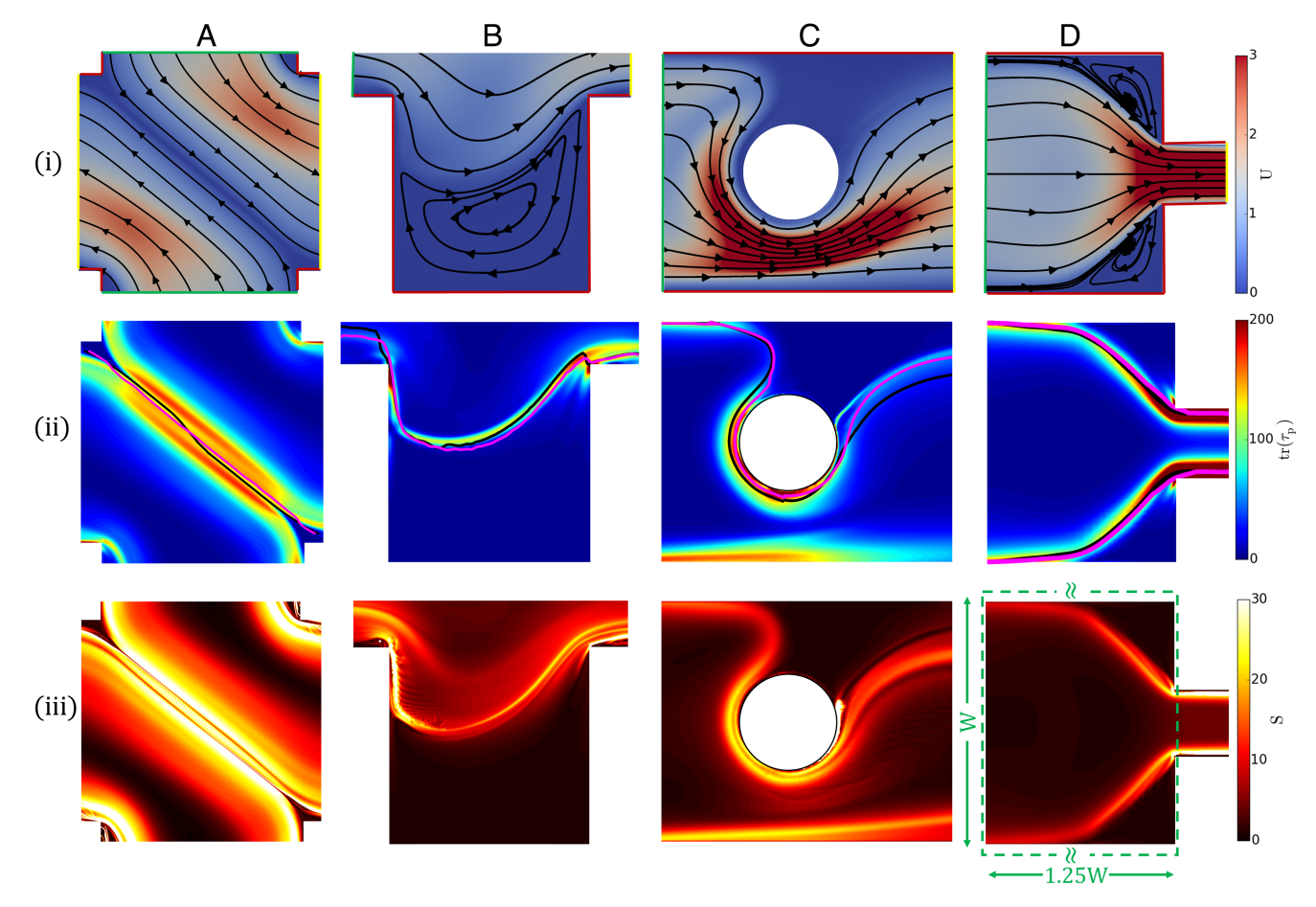
The stress field grows quadratically with Wi for both the shear and extensional flows (*SI Appendix*). However, the stretching field at a large Wi grows linearly with Wi for shear flows, whereas it grows exponentially for linear extensional flow, leading to the slower growth of  $\operatorname{tr}(\tau_p)$  with S in the extensional flow than in the shear flows.

Thus,  $\operatorname{tr}(\tau_p)$  and S are related by compact analytical expressions for different steady (Eq. 5) and weakly unsteady (Eq. 12) flows of the ordered fluid model at Wi  $\ll$  1 and MWCSH flows at Wi < 1. Further, the analysis of flows undergoing MWCSH uncovers exact relationships between  $\operatorname{tr}(\tau_p)$  and S at Wi  $\gg$  1 for shear (Eq. 15) and extensional (Eq. 16) flows (SI Appendix). These results clearly illustrate a deepseated quantitative relationship between the polymeric stress and Lagrangian stretching history, which links the topologies of these fields. However, in general, for flows having mixed kinematics, such exact expressions at Wi > 1 are not accessible. Hence, we use numerical simulations to further explore the relationship between the stress and stretching fields in complex geometries at large Wi.

Numerical Simulations of Stress and Stretching for Strongly Viscoelastic Flows. Beyond the exact analytical correspondence between stress and stretching for weakly unsteady viscoelastic flows (Eqs. 12, 15, and 16), strong nonlinearities yield complex

and time-dependent flow structures that emerge at a large Weissenberg number (13, 17, 18). To illustrate the persistent concordance between the polymeric stress and stretching field topologies, viscoelastic flows are numerically simulated through various geometries at large Weissenberg numbers (Wi  $\gtrsim 1$ ), and the polymeric stress and stretching fields are obtained numerically (Materials and Methods). At a large Weissenberg number, the Lagrangian stretching field mirrors the stress field topology across four different benchmark geometries (Fig. 1). For Wi > Wi<sub>cr</sub>, strong flow asymmetries develop in the hyperbolic base flow of the cross-slot geometry (Fig. 1 A(i)) (24, 41) as well as in the flow past a confined cylinder (Fig. 1 C(i)) (42). Despite the otherwise creeping flow conditions, viscoelasticity leads to flow separation in the corners upstream of an isolated constriction (Fig. 1 D(i)) (43) as well as an unsteady asymmetric eddy in the flow over a cavity (Fig. 1 B(i)). For all four geometries, the stretching field (Fig. 1(iii)) has a strong correlation with the topology of the stress field (Fig. 1(ii)) and SI Appendix, Fig. S6, which are characterized by thin streaks with high values of S and  $tr(\tau_p)$ , respectively. These features indicate regions where polymers have experienced significant deformation—and thus, stress—due to the integrated effects of shear and extensional flow over the past  $\Delta t = \lambda$ . Our observations persist in threedimensional flows (SI Appendix, Fig. S7) and are independent of the rheological model (SI Appendix, Fig. S8). The (attractive or unstable) stretching manifolds were extracted from the ridges of the maximal stretching for different integration times ( $\Delta t =$ λ, 2λ; Fig. 1(iii) and SI Appendix, Fig. S5) and superimposed on the stress field (Fig. 1(ii)). In line with their known behavior as strong transport barriers, these material lines act as separatrices between regions with disparate flow characteristics, including asymmetric flows (Fig. 1 A and C) and separated eddies (Fig. 1 B and D). While the magnitude of stretching increases with the integration time (SI Appendix, Fig. S5), the position of the stretching manifolds exhibits minimal change for  $\Delta t > \lambda$ , and they remain coincident with streaks of the stress fields (Fig. 1, Row (ii)).

Beyond comparing their respective topologies, numerical simulations of viscoelastic flows enable us to further investigate the relationship between the magnitude of the stress and stretching fields. As an illustrative example, we consider the spatial average of the stress,  $\langle \operatorname{tr}(\boldsymbol{\tau}_{\boldsymbol{p}}) \rangle$ , and stretching,  $\langle S \rangle$ , over a fixed region of space (Fig. 2) within the constriction flow (Fig. 1 D(iii)), green box. For small Weissenberg number, the predicted scaling



Flow field (Row i), trace of the polymeric stress tensor (Row ii), and stretching field (Row iii) for viscoelastic flows in different geometries at large Weissenberg numbers (Wi  $\gtrsim$  1): (Column A) cross-slot geometry at Wi = 4, (Column B) flow over a cavity at Wi = 1.25, (Column C) cylinder confined in a channel at Wi = 2.5, and (Column D) flow through an isolated constriction at Wi = 0.75. Wi =  $\lambda U_{in}/L_C$ , where  $U_{in}$  is the inlet velocity of the geometry. The characteristic length scale, L<sub>C</sub>, for the geometries is the upstream channel width (A and D), the channel width at the cavity (B), and the cylinder diameter (C). The velocity U is normalized by  $U_{in}$ , and the stress  $\tau p$  is normalized by  $\eta_0 U_{in}/L_c$ , where  $\eta_0$  is the zero-shear rate viscosity of the viscoelastic fluid. Black and magenta lines (Row ii) are the stretching manifolds (ridge of maximal stretching) obtained from stretching fields (Row iii and SI Appendix, Fig. S5) for integration time intervals of  $\Delta t = \lambda$  and  $\Delta t = 2\lambda$ , respectively. The stretching fields shown (Row iii) correspond to  $\Delta t = \lambda$ . No-slip boundaries are highlighted by red lines, whereas inlets and outlets are indicated by green and yellow, respectively (Row i). Geometries shown are a small portion of larger simulation domains, which ensured sufficient entrance and exit lengths.

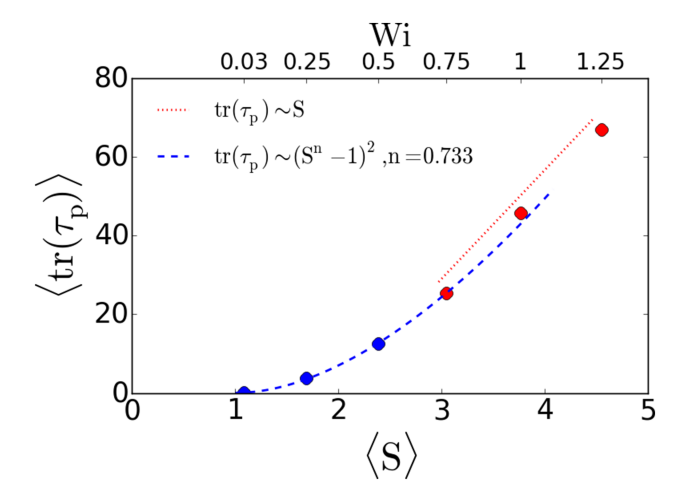


**Fig. 2.** Mean stress increases with mean stretching ( $\Delta t = \lambda$ ) for a viscoelastic flow through an isolated constriction (Fig. 1*D*) at different Wi. The region 1.25W × W upstream of the constriction (Fig. 1 *D*(iii)), green box, where W is the upstream width of the channel, is used to calculate the spatial average of stress and stretching. The stress  $\tau_{p}$  is normalized by  $\eta_{0}U_{in}/L_{c}$  corresponding to Wi = 0.75.

 ${\rm tr}(\pmb{\tau_p}) \sim (S^n-1)^2$  (Eq. 5) is recovered as Wi  $\to 0$  (Fig. 2, blue), similar to the scaling between the local values of stress and stretching fields (*SI Appendix*, Fig. S10). At large Wi,  $\langle {\rm tr}(\pmb{\tau_p}) \rangle$  and  $\langle S \rangle$  exhibit a linear scaling (Fig. 2, red), which we hypothesize is due to the highly mixed flow kinematics upstream of the constriction (*SI Appendix*, Fig. S1): In this regime, the slope of the curve of  ${\rm tr}(\pmb{\tau_p})$  vs S increases with S for shear deformation (Eq. 15) but decreases for extensional deformation (i.e., for S > e) (Eq. 16). In this example, the quantitative relationship between the stress and stretching fields is obtained along with their topological resemblance. However, the scaling exponent is

not universal (*SI Appendix*, Fig. S10), and developing a robust general predictive framework for relating  $\operatorname{tr}(\tau_p)$  and *S* will require further investigation.

**Extension to Complex Geometries.** Intricate flow geometries for example, in porous media (8)—increase the complexity of instabilities leading to multistable and strongly time-dependent flow structures (17, 18, 44). Here, we compare the polymeric stress field and Lagrangian stretching field for topologically complex and unsteady flows stemming from multiple cylinders (18, 44) and constrictions (17). The addition of a second cylinder in a steady channel flow leads to two transitions with increasing Wi (18, 44): At the first transition, the elastic wake downstream of the first cylinder bifurcates, yielding two symmetric eddies (Fig. 3 A(i)) encircled by streaks of high stress (Fig. 3 A(ii)). At the second transition, the stress topology becomes asymmetric (Fig. 3 B(ii)), and the flow is diverted to one side of the cylinders (Fig. 3 B(i)). Subsequent to each transition, ridges of S (Fig. 3 A(iii) and B(iii)) coincide with regions of high  $tr(\tau_p)$ (Fig. 3 A(ii) and B(ii)), whereby the stretching manifolds isolate the regions of vortical and quiescent flow from the bulk. Finally, viscoelastic instability in flow through a series of interconnected pores and throats leads to fluctuating flow patterns (Fig. 3 C(i)) and SI Appendix, Fig. S9, (17). Flow separation in the high-stress throat (Fig. 3 C(ii)) causes eddy formation in different regions of the pores, corresponding to four distinct flow patterns (Fig. 3 C(i)). For large Wi, advection of the stressed polymers spans multiple pores, and consequently, the Lagrangian stretching field exhibits a richer topology (Fig. 3 C(iii)). However, the LCSs expected to dominate the dynamics are the strongest local stretching lines (29), which indeed correspond to ridges in the stress field (Fig. 3 C(ii)). The secondary ridges and finer structures in the stretching field of unsteady flows (Fig. 3 C(iii)) emerge due to mixed kinematics (SI Appendix, Fig. S2), and they are

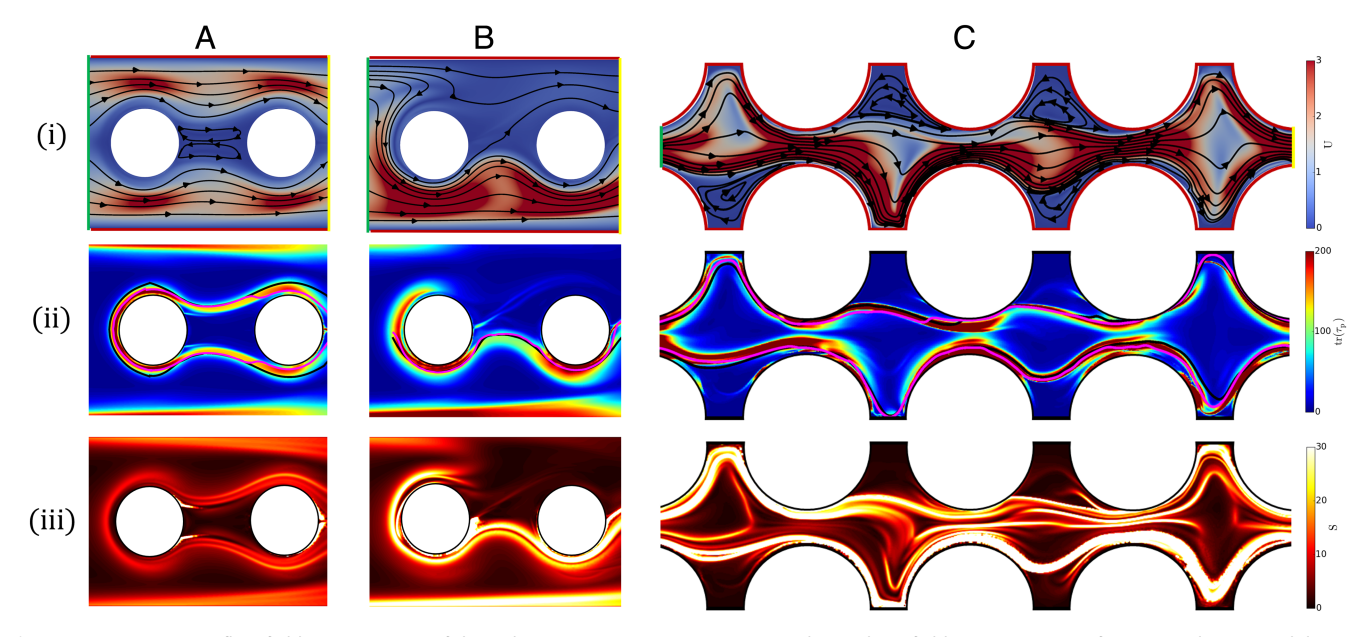


Fig. 3. Instantaneous flow field (Row i), trace of the polymeric stress tensor (Row i), and stretching field (Row i) arising from viscoelastic instabilities in flows with two cylinders aligned in the streamwise direction in a channel with moderate and large Weissenberg number, Wi = 1.88 (Column A) and Wi = 3.12 (Column B), and in a corrugated channel with Wi = 1.68 (Column C) (SI Appendix, Fig. S9). Wi =  $\lambda U_{in}/L_C$ , where  $L_C$  is the cylinder diameter in (A) and (B) and the pore half-width in (C). The velocity U and stress  $\tau_p$  are normalized by  $U_{in}$  and characteristic shear stress ( $\eta_0 U_{in}/L_C$ ), respectively. Black and magenta lines (Row ii) represent the stretching manifolds (ridge of maximal stretching) obtained from stretching fields (SI Appendix, Fig. S5, Row iii) for integration time intervals of  $\Delta t = \lambda$  and  $\Delta t = 2\lambda$ , respectively. The stretching fields shown (Row ii) correspond to  $\Delta t = \lambda$ . No-slip boundaries are highlighted by red lines, whereas inlets and outlets are green and yellow, respectively (Row i). Geometries shown are a small portion of larger simulation domains, which ensured sufficient entrance and exit lengths.

further refined with increasing integration time ( $\Delta t$ ; *SI Appendix*, Fig. S5). However, the maximum attractive (unstable) material lines (strongest ridges), which control the flow states, remain nearly unchanged (Fig. 3 C(ii)).

At large Wi, despite the excellent agreement between the stress field and stretching field in the regions of high stress, subtle differences also persist in other regions (Fig. 3 C(ii) and (iii)). The regions where streaks of high polymeric stress form are largely shear-dominated (SI Appendix, Figs. S1 and S2), as they act as barriers to flow crossing and exist between regions of strong extensional or vortical flow (17). The theoretical analysis of MWCSH flows has shown that there exists a direct relationship between the stress and stretching for both homogeneous and nonhomogeneous shear flows at Wi  $\gg 1$  (Eq. 15). Taken together, these results illustrate the origin of the strong correlation between the stress and stretching fields in the regions of high stress. In contrast, mixed-kinematics regions away from highstress zones (SI Appendix, Figs. S1 and S2) include extensional flow components with a different stress-stretching scaling at Wi > 1 (Eqs. 15 and 16). Detailed numerical analysis supports this observation and indicates decreased correlation between the stress and stretching fields as mixed kinematics emerge in strong flows (Wi  $\gtrsim O(1)$ ; *SI Appendix*, Figs. S3 and S4).

### **Conclusions**

Knowledge of the stress field is essential to elucidate the emergent flow patterns and transport properties in viscoelastic flows. The work presented here applies concepts from Lagrangian coherent structures to gain insights into the often Eulerian framework of viscoelastic fluid mechanics, thus bringing together two disparate fields of continuum analysis. In doing so, we show that the stretching field, which depends only on the flow kinematics, is a powerful indicator of the topology of the underlying polymeric stress field. For small Wi, we analytically derived a general relationship between the trace of polymeric stress tensor and the Lagrangian stretching field, and for unstable flows at large Wi, numerical simulations show a strong correlation between the stress topology and manifolds of the stretching field. The extension of these results to three dimensions provides copious opportunities for future investigations. An important outcome of this work is the potential to determine the stress field topology directly from conventional experimental velocimetry data for arbitrary viscoelastic materials and flow geometries. LCSs that underlie turbulent and chaotic flows are known to regulate material transport, and anomalous transport effects often arise from unstable polymeric flows (8, 45). The concepts established

- K. S. Sorbie, Polymer-Improved Oil Recovery (Springer Science & Business Media, 2013).
- R. Tang et al., Direct delivery of functional proteins and enzymes to the cytosol using nanoparticlestabilized nanocapsules. ACS Nano 7, 6667-6673 (2013).
- M. Thiébaud, Z. Shen, J. Harting, C. Misbah, Prediction of anomalous blood viscosity in confined shear flow. Phys. Rev. Lett. 112, 238304 (2014).
- M. Kumar, J. S. Guasto, A. M. Ardekani, Transport of complex and active fluids in porous media. J. Rheol. 66, 375-397 (2022).
- C. A. Browne, S. S. Datta, Elastic turbulence generates anomalous flow resistance in porous media Sci. Adv. 7 (2021).
- M. M. Denn, Fifty years of non-Newtonian fluid dynamics. AIChE J. 50, 2335-2345 (2004).
- P. Stoodley, I. Dodds, D. De Beer, H. L. Scott, J. D. Boyle, Flowing biofilms as a transport mechanism for biomass through porous media under laminar and turbulent conditions in a laboratory reactor system. Biofouling 21, 161-168 (2005).
- D. M. Walkama, N. Waisbord, J. S. Guasto, Disorder suppresses chaos in viscoelastic flows. Phys. Rev. Lett. 124, 164501 (2020).
- S. J. Haward, C. C. Hopkins, A. Q. Shen, Stagnation points control chaotic fluctuations in viscoelastic porous media flow. *Proc. Natl. Acad. Sci. U.S.A.* **118**, e2111651118 (2021).
- J. D. Jacob, R. Krishnamoorti, J. C. Conrad, Particle dispersion in porous media: Differentiating effects of geometry and fluid rheology. Phys. Rev. E 96, 1-13 (2017).
- 11. C. E. Wagner, G. H. McKinley, The importance of flow history in mixed shear and extensional flows. J. Non-Newtonian Fluid Mech. 233, 133-145 (2016).

here show intriguing links between polymeric stress and stretching kinematics, which could prove useful in investigating the dynamics and transport for a range of applications from mixing to natural flows (2, 8, 16, 46).

#### **Materials and Methods**

Polymeric Stress in Simulations. The polymeric stress tensor is calculated using the FENE-P constitutive model, which captures fluid elasticity and shearthinning behaviors as well as the finite stretching of the polymeric chains (47):

$$\boldsymbol{\tau}_{p} + \frac{\lambda}{f} \overset{\nabla}{\boldsymbol{\tau}}_{p} = \frac{a\eta_{p}}{f} (\nabla \mathbf{u} + \nabla \mathbf{u}^{\mathsf{T}}) - \frac{D}{Dt} \left(\frac{1}{f}\right) [\lambda \boldsymbol{\tau}_{p} + a\eta_{p} \mathbf{I}], \quad [17]$$

where  $\eta_{
m p}$  is the polymeric contribution to the zero-shear rate viscosity of the fluid.  $\overset{\vee}{\tau}_p$  is given by:

$$\overset{\nabla}{\boldsymbol{\tau}}_{\rho} = \frac{D\boldsymbol{\tau}_{\rho}}{Dt} - \boldsymbol{\tau}_{\rho} \cdot \nabla \mathbf{u} - \nabla \mathbf{u}^{\mathsf{T}} \cdot \boldsymbol{\tau}_{\rho}, \tag{18}$$

and the nonlinear function f is

$$f(\tau \mathbf{p}) = \frac{L^2 + \frac{\lambda}{\partial \eta_p} tr(\tau \mathbf{p})}{L^2 - 3},$$
 [19]

where  $a = L^2/(L^2 - 3)$ , and L is the maximum extensibility of the polymeric chains. Numerical simulations are implemented using OpenFOAM (48) and RheoTool (49). The log-conformation method is used to solve for the logarithm of the conformation tensor  $(\Theta)$  (49, 50), and then, the polymeric stress tensor is determined using

$$au_{p} = \frac{\eta_{p}}{\lambda} (fe^{\Theta} - aI).$$
 [20]

**Stretching Field in Simulations.** The stretching field (S) is also calculated numerically from the simulated velocity field: Four auxiliary points centered around each primary grid point define a fluid element. The flow map  $(\Phi)$ is obtained by numerically integrating the auxiliary point in time, and the deformation-gradient tensor  $(\nabla \Phi)$  on each primary grid point is computed by central differencing of the auxiliary points (51).

Data, Materials, and Software Availability. All study data are included in the article and/or SI Appendix.

**ACKNOWLEDGMENTS.** We thank D.M. Walkama for helpful discussions. This work was supported by National Science Foundation awards CBET-1700961, CBET-1705371, and CBET-2141404 (to A.M.A.), and CBET-2141349, CBET-1701392, and CAREER-1554095 (to J.S.G.).

- 12. R. G. Larson, Instabilities in viscoelastic flows. Rheol. Acta 31, 213-263 (1992).
- 13. P. Pakdel, G. H. McKinley, Elastic instability and curved streamlines. Phys. Rev. Lett. 77, 2459-2462 (1996).
- P. E. Arratia, C. C. Thomas, J. Diorio, J. P. Gollub, Elastic instabilities of polymer solutions in crosschannel flow. Phys. Rev. Lett. 96, 12-15 (2006).
- 15. A. Groisman, V. Steinberg, Elastic turbulence in a polymer solution flow. *Nature* **405**, 53–55 (2000).
- 16. A. Groisman, V. Steinberg, Efficient mixing at low Reynolds numbers using polymer additives. Nature 410, 905-908 (2001).
- 17. M. Kumar, S. Aramideh, C. A. Browne, S. S. Datta, A. M. Ardekani, Numerical investigation of multistability in the unstable flow of a polymer solution through porous media. Phys. Rev. Fluids 6, 033304 (2021).
- M. Kumar, A. M. Ardekani, Elastic instabilities between two cylinders confined in a channel. Phys. Fluids 33, 074107 (2021).
- 19. G. R. Moss, J. P. Rothstein, Flow of wormlike micelle solutions through a periodic array of cylinders. J. Non-Newtonian Fluid Mech. 165, 1-13 (2010).
- C. li Sun, H. Y. Huang, Measurements of flow-induced birefringence in microfluidics. *Biomicrofluidics* **10**, 1–13 (2016).
- 21. G. G. Fuller, Optical Rheometry of Complex Fluids (Oxford University Press on Demand, 1995).
- D. B. Murphy, Fundamentals of Light Microscopy and Electronic Imaging (John Wiley & Sons, 2002).
   T. J. Ober, J. Soulages, G. H. McKinley, Spatially resolved quantitative rheo-optics of complex fluids in a microfluidic device. J. Rheol. 55, 1127-1159 (2011).

- S. J. Haward, G. H. Mckinley, A. Q. Shen, Elastic instabilities in planar elongational flow of monodisperse polymer solutions. Sci. Rep. 6, 1–18 (2016).
- D. E. Smith, H. P. Babcock, S. Chu, Single-polymer dynamics in steady shear flow. Science 283, 1724–1727 (1999).
- D. Kawale et al., Polymer conformation during flow in porous media. Soft Matter 13, 8745–8755 (2017).
- G. Haller, Distinguished material surfaces and coherent structures in three-dimensional fluid flows. Phys. D: Nonlinear Phenom. 149, 248–277 (2001).
- G. A. Voth, G. Haller, J. P. Gollub, Experimental measurements of stretching fields in fluid mixing. Phys. Rev. Lett. 88, 4 (2002).
- 29. G. Haller, Lagrangian coherent structures. Ann. Rev. Fluid Mech. 47, 137-162 (2015).
- S. Parsa et al., Rotation and alignment of rods in two-dimensional chaotic flow. Phys. Fluids 23, 043302 (2011).
- A. Dehkharghani, N. Waisbord, J. Dunkel, J. S. Guasto, Bacterial scattering in microfluidic crystal flows reveals giant active Taylor-Aris dispersion. *Proc. Natl. Acad. Sci. U.S.A.* 116, 11119–11124 (2019).
- P. E. Arratia, G. A. Voth, J. P. Gollub, Stretching and mixing of non-Newtonian fluids in timeperiodic flows. *Phys. Fluids* 17, 053102 (2005).
- W. Noll, Motions with constant stretch history. Arch. Ration. Mech. Anal. 11, 97–105 (1962).
- R. B. Bird, R. C. Armstrong, O. Hassager, Dynamics of Polymeric Liquids. Vol. 1: Fluid Mechanics (1987).
- J. M. Dealy, Weissenberg and deborah numbers-their definition and use. Rheol. Bull. 79, 14–18 (2010).
- R. H. Éwoldt, G. H. McKinley, Mapping thixo-elasto-visco-plastic behavior. Rheol. Acta 56, 195–210 (2017).
- R. R. Huilgol, On the properties of the motion with constant stretch history occurring in the Maxwell rheometer. Trans. Soc. Rheol. 13, 513–526 (1969).

- 38. R. R. Huilgol, Algorithms for motions with constant stretch history. Rheol. Acta 15, 120-129 (1976).
- 39. R. R. Huilgol, A class of motions with constant stretch history. Q. Appl. Math. 29, 1-15 (1971).
- W. Noll, A mathematical theory of the mechanical behavior of continuous media. Arch. Ration. Mech. Anal. 2, 197–226 (1958).
- R. J. Poole, M. A. Alves, P. J. Oliveira, Purely elastic flow asymmetries. Phys. Rev. Lett. 99, 1-4 (2007).
- S. Varchanis, C. C. Hopkins, A. Q. Shen, J. Tsamopoulos, S. J. Haward, Asymmetric flows of complex fluids past confined cylinders: A comprehensive numerical study with experimental validation. *Phys. Fluids* 32, 053103 (2020).
- A. Lanzaro, X. F. Yuan, Effects of contraction ratio on non-linear dynamics of semi-dilute, highly polydisperse PAAm solutions in microfluidics. J. Non-Newtonian Fluid Mech. 166, 1064–1075 (2011).
- A. Varshney, V. Steinberg, Elastic wake instabilities in a creeping flow between two obstacles. *Phys. Rev. Fluids* 2, 051301 (2017).
- S. Yamani et al., Spectral universality of elastoinertial turbulence. Phys. Rev. Lett. 127, 074501 (2021).
- S. S. Suarez, A. A. Pacey, Sperm transport in the female reproductive tract. Hum. Reprod. Update 12, 23–37 (2006).
- R. B. Bird, C. F. Curtiss, R. C. Armstrong, O. Hassager, Dynamics of Polymeric Liquids, Volume 2: Kinetic Theory (Wiley, 1987).
- 48. H. Jasak, A. Jemov, Z. Tukovic, "Openfoam: A C++ library for complex physics simulations" in
- International Workshop on Coupled Methods in Numerical Dynamics (2007), pp. 1–20.
  49. F. Pimenta, M. A. Alves, Stabilization of an open-source finite-volume solver for viscoelastic fluid
- flows. *J. Non-Newtonian Fluid Mech.* **239**, 85–104 (2017). 50. R. Fattal, R. Kupferman, Constitutive laws for the matrix-logarithm of the conformation tensor. *J. Non-Newtonian Fluid Mech.* **123**, 281–285 (2004).
- K. Onu, F. Huhn, G. Haller, L. C. S. Tool, A computational platform for Lagrangian coherent structures. J. Comput. Sci. 7, 26-36 (2015).